Crystal-melt and melt-vapor interfaces of nickel

E. T. Chen, R. N. Barnett, and Uzi Landman
School of Physics, Georgia Institute of Technology, Atlanta, Georgia 30332-0430
(Received 14 February 1989)

The equilibrium crystal-to-melt interfaces for Ni(001) and Ni(111) and the melt-to-vapor interface are investigated at the melting point, with use of molecular-dynamics simulations and the embedded-atom method. The melting temperature of nickel determined from these simulations is 1733±22 K, in good agreement with the experimental value. The crystal-to-melt interface is found to be characterized by liquid layering, with properties such as structural order parameters and diffusion coefficients varying gradually across the transition region. The transition region extends over several layers and is more diffuse at the (001) interface. At the melt-to-vapor interface the density increases, driven by an increase in the magnitude of the density-dependent embedding-energy contribution to the cohesive energy of the metal. This behavior is in contrast to that found at the melt-to-vapor interface of nonmetallic systems.

I. INTRODUCTION

Knowledge of the structural, dynamical, and energetic properties of interphase interfaces is of fundamental importance in developing basic understanding of a number of material systems and phenomena such as phase transformations (crystal growth and melting), wetting, and interfacial phenomena (e.g., electrochemical processes). Consequently, significant theoretical[1–6] and experimental[3,6–8] efforts have been directed towards enhancing our understanding of the properties of a variety of such interfacial systems (i.,e., crystal-melt, liquid-vapor interfaces).

A theoretical framework for treating the equilibrium thermodynamics of interfaces in general was introduced by Gibbs in 1878.[9] Modern theoretical investigations in this area focus on the development of statistical-mechanical methods,[1,3,5,10–14] specifically formulated for treating inhomogeneous systems, and numerical simulations[1–5,15–27] which allow studies with refined spatial and temporal resolution.

The crystal-melt interface presents a particularly challenging problem because the interface is confined between two condensed phases (solid and liquid) and thus is not easily probed experimentally. In addition, the inhomogeneity of the system, in particular the narrow spatial extent of the interfacial transition region in comparison to the dimensions of the two interfacing bulk phases, and the complex nature of the phases (in particular the liquid) make theoretical treatments rather difficult. Consequently, most theoretical studies of this interface employed model systems characterized by simple interatomic potentials (usually pairwise interactions of simple functional forms).

An important issue which underlies many studies of materials is the relationship between the properties of the system and the nature of the intermolecular potentials (i.e., energetics) between the atomic or molecular constituents. In this regard solid-to-melt interfaces in metallic systems present a complex situation due to the density dependence of interactions which underlies the cohesion of these materials. Thus, the inherent inhomogeneity at the interfacial region, coupled with the complex nature of the energetics of metals cause theoretical studies of these systems to be particularly difficult. Nevertheless, for simple metals (e.g., free-electron metals) formulations based on density-dependent expressions for the total energy[28–30] (employing effective Hamiltonians within the context of pseudopotential theory) have been used with some success.[5,29–31]

In this study we investigate, using molecular-dynamics (MD) simulations, the crystal-melt and melt-vapor interfaces of nickel. Since the effective Hamiltonian formulations based on second-order perturbation theory with respect to the electron-ion interaction are limited to free-electron (*sp*-bonded) metals, we have represented the energetics of the material using the embedded-atom method (EAM)[32] which has been recently applied with significant success in studies of various transition-metal systems. Following a brief description in Sec. II of the EAM and the MD simulation method, we present in Sec. III results for the equilibrium (001) and (111) crystal-melt and for the liquid-metal–vapor interfaces of Ni. Our results are summarized in Sec. IV.

II. METHOD

The embedded-atom method (EAM)[32] is a semiempirical method which provides a convenient framework for atomistic calculations of metallic systems. In this method the dominant contribution to the energy of the metal is viewed as the energy to embed an atom into the local electron density provided by the other atoms of the system, represented by an embedding-energy function F, which is supplemented by short-range, two-body interactions due to core-core repulsion, ϕ. The basic idea underlying this method is thus the same as that which motivated the development of the earlier effective-medium theory (EMT),[33] and both find their roots in the density-functional theory.[34]

The cohesive energy $E_{\rm coh}$ of the metal is given in EAM

by the *ansatz*

$$E_{\text{coh}}=\sum_i F_i\left[\sum_{j(\neq i)}\rho_j^a(R_{ij})\right]+\tfrac{1}{2}\sum_{\substack{i,j\\(i\neq j)}}\phi_{ij}(R_{ij})\ , \qquad (1)$$

where ρ^a is the spherically averaged atomic electron density, and R_{ij} is the distance between atoms i and j located at $\mathbf{R}_i$ and $\mathbf{R}_j$. Thus the background density for each atom i is determined as the superposition of atomic density tails from the other atoms, evaluated at the nucleus of the ith atom. In the EAM the functions F and ϕ are determined by choosing for them functional forms which meet certain general requirements, and fitting parameters in these functions to a number of bulk equilibrium properties of the solid such as lattice constant, heat of sublimation, elastic constants, vacancy-formation energy, etc. From the several parametrization procedures which have been discussed,[32] we have chosen the one described by Foiles[35] in his study of liquid transition metals.

The total energy expression, given in Eq. (1), with the above parameterization, is then employed in a molecular-dynamics simulation in which the temporal evolution of the system is followed via integration of the classical equations of motion of the atoms. In our molecular-dynamics simulations the semi-infinite system is modeled via a thick slab of interacting dynamic particles which in addition interact with several crystalline layers of a static substrate in the desired crystallographic orientation. Thus in these simulations periodic boundary conditions are imposed only in directions parallel to the surface plane. Due to the short range of the repulsive pair interactions and the finite range of the atomic charge densities it is sufficient to represent the static substrate by three solid layers. The lattice constant of the static substrate, and thus the dimensions of the calculational cell in the directions parallel to the surface plane, is appropriate for the temperature of the study [determined via constant pressure simulations of the bulk solid,[36] i.e., three-dimensional periodic boundary condition, at the required temperature and external pressure (in our case $p_{\text{ext}}=0$)].

In the first stage of the simulation we prepare a crystalline solid consisting of N_l layers with n_l particles in each layer, equilibrated at a high temperature of 1650 K [below the experimental melting point (1725 K) of the bulk solid[37]]. In this initial preparation stage a lattice constant of 3.585 Å, determined from a separate bulk simulation at 1700 K, was used, and the simulations were performed at constant temperature, using the macrocanonical ensemble method[38] (i.e., stochastic thermalization of particle velocities). For both the Ni(001) and Ni(111) systems equilibration runs for 8×10^3 Δt were performed (the integration time step $\Delta t=1.038\times10^{-15}$ sec). Further heating of the system (via stochastic collisions, or scaling of particle velocities) results in melting of the system starting from the free surface. When a portion of the system melts, the heat control is stopped and the system continues to evolve as a microcanonical ensemble (i.e., constant-energy simulation). Alternatively, starting from the solid at 1650 K, one can add enough energy ΔE to the system (by scaling of particle velocities) to raise the temperature to the experimental melting point (1725 K) and to melt a desired number of layers. To estimate the amount of energy ΔE estimates of the specific heat and latent heat of the system (obtained from experimental data or separate simulations) are used. In the final-preparation stage the system is allowed to evolve as a microcanonical ensemble (i.e., constant-energy simulation) until the equilibrium state is established in which a solid portion of the system coexists with its melt.

In our studies we have experimented with both methods of preparation, starting from the solid below the melting point (i.e., 1650 K). Both methods yield the same final state provided that the constant-energy stage is run for a sufficient amount of time. The criteria which we used in order to determine that the equilibrium state of the solid-melt system was achieved in the constant-energy stage of the simulation are (a) absence of secular trends versus time in the kinetic energy and in the contributions to the potential energy, (b) a uniform profile of the kinetic temperature across the system [see Figs.1(b) and 2(b) for Ni(001) and Ni(111), respectively], (c) absence of variations in the layer diffusion coefficients (see Sec. III B) calculated for different segments of time, and (d) absence of periodic oscillations of interlayer spacing and registry in the crystalline part of the system. To satisfy these equilibrium criteria the system was allowed to evolve in the constant-energy stage for a prolonged period of time; 3×10^4 $\Delta t=31.14$ ps for the Ni(001) system and 5.4×10^4 $\Delta t=56.05$ ps for the Ni(111) system. The results which we present are time averages of the systems' properties performed over 2×10^4 $\Delta t=20.76$ ps, following the constant-energy equilibration discussed above, with the system at the equilibrium coexistence state.

In order to investigate the crystalline face dependence of the crystal to melt interface we have simulated two nickel systems: (a) Ni(100), with $N_l=25$ and $n_l=50$ atoms/layer (i.e., total number of dynamic particles, $N=1250$), and (b) Ni(111), with $N_l=21$, $n_l=56$ atoms/layers ($N=1176$). The equations of motion were integrated using the velocity form of the Verlet algorithm[38] with a time step of 1.038×10^{-15} sec, which proved to allow energy conservation to better than five, a significant figure over extended periods.

III. RESULTS

A. Melting temperature

Since the EAM potentials which we used were parametrized via fitting to a number of properties of bulk solid Ni and have been shown to provide an adequate description of the liquid,[35] it is of interest to determine the melting temperature T_m obtained in simulations with these potentials. In Figs. 1 and 2, equilibrium (at crystal-melt coexistence) time-averaged profiles along the direction normal to the crystalline plane z are shown for the particle density (ρ), kinetic energy (E_k), and kinetic temperature [$T=(2/3N)E_k$], total energy (E_{tot}), and of the pair-potential (E_{pair}) and embedding-energy ($E_{\text{embedding}}$) contributions, for the Ni(100) and Ni(111) systems, respectively (in these profiles properties of only the dynamic slab portion of the system are included).

As seen from Figs. 1(b) and 2(b) the average tempera-

ture is uniform throughout the system (as is required in equilibrium) from which we determine $T_m = 1733$ K$\pm$22 K (the estimated error is an upper bound) in good agreement with the experimental[37] bulk melting temperature ($T_m = 1725$ K). We should note here that we have separately studied[39] the dynamics of the melting process of surfaces of Ni at various crystallographic orientations and have found evidence for surface premelting phenomena, particularly noticeable for the (110) surface.

From the profiles of the density and total energy per atom [Figs. 1(a) and 1(c) and 2(a) and 2(c)] we can estimate the latent heat of melting as the difference between the average energies in the solid and liquid regions. The value thus obtained 0.19 eV/atom is in good agreement with the experimental value[37] for Ni 0.182 eV/atom.

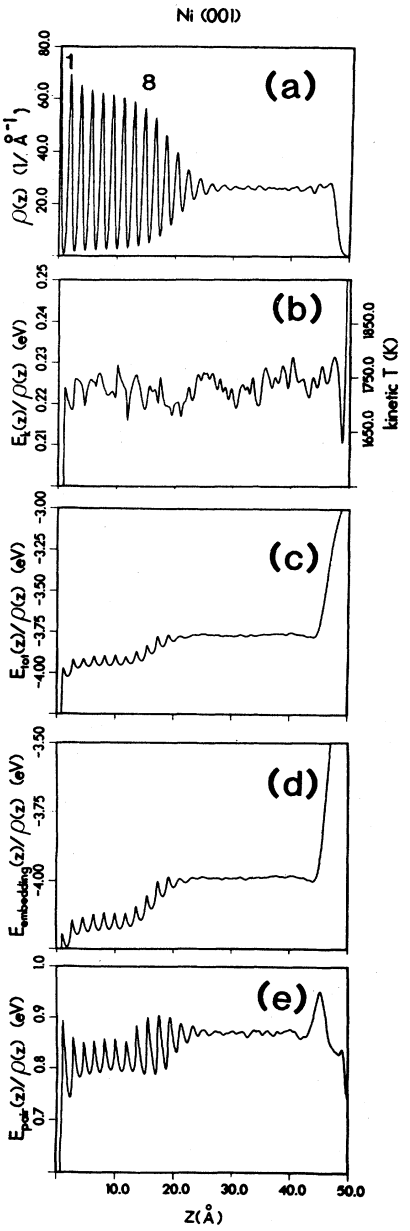

FIG. 1. Equilibrium profiles of the Ni(001) system at the melting point vs distance z normal to the (001) plane (a) density ρ; (b) kinetic energy E_k normalized by the density, and kinetic temperture T (right-hand-side scale); (c) per-particle total energy $E_{\rm tot}$; (d) per-particle embedding energy [see Eq. (1) first term on rhs]; (e) pair-interaction energy [see Eq. (1), second term on rhs]. Energies and distances in units of eV and Å, respectively. Temperature in degrees K. The first dynamic layer is at $z = 1.792$ Å. The first and eighth dynamic layers are labeled (a). Note the layered structure at the solid-melt interface and the increase in density in the melt-vapor interface.

B. Interfacial structure and dynamics

1. Solid-to-melt interface

Having determined the melting temperature we focus in the rest of the paper on the structural, energetic, and

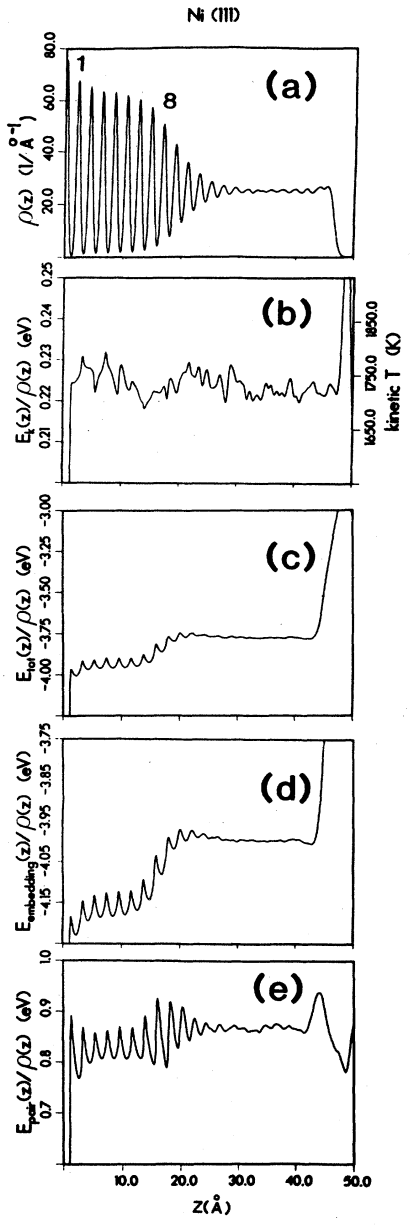

FIG. 2. Same as Fig. 1 for the Ni(111) system. The first dynamic layer is at 2.067 Å. The first and eighth dynamic layers are labeled (a).

dynamic properties of the system. First we discuss the solid-to-melt interface.

As seen from the density and energy profiles in Figs. 1 and 2 the systems exhibit two phases (a solid and a liquid) and two interphase interfaces (solid melt and melt vapor). The maxima in the density profiles [Figs. 1(a) and 2(a)] correspond to layer positions, which correspond to the minima in the energy profiles. Furthermore, the solid-melt interface is diffuse exhibiting a gradual transition in properties from solid to the melt. We note in particular the dominant contribution of the embedding energy [Figs. 1(d) and 2(d)] to the total energy (per atom) and the monotonic transition from solid to liquid, reflecting the spatial variation of the electron density. In this context we remark that the division of the cohesive energy into embedding and pair-interaction contributions [Eq. (1)] is nonunique. Therefore, comments about the behavior of *individual* contributions to the total energy, are within the context of the parametrization which we employed.[35]

The dependence of the nature of the crystalline to melt transition on the crystallographic orientation of the interface is demonstrated in Fig. 3 where the density and total energy profiles in the vicinity of the Ni(001) interface (solid) and the Ni(111) interface (dashed) are shown. In drawing these figures the profiles for the two systems were aligned such that the location of the 11th layer of the (001) system coincides with the location of the 10th layer of the (111) system. As seen, while for $z \geq 20$ Å the profiles continue to be aligned (i.e., extrema occur at about the same distances for the two systems) with a spacing between extrema corresponding to roughly the interlayer distance between (111) crystalline planes ($d_{(111)}=2.067$ Å for $z \leq 20$ Å), the profiles for the (001) system shift with respect to those of the (111) system. Furthermore, while in the (111) profiles the periodicity along the z axis is maintained with a spacing equal to $d_{(111)}$ throughout, for the (001) system the periodicity gradually changes, from $d_{(001)}=1.792$ Å (the spacing between adjacent crystalline layers) for small z to $d_{(111)}$ for $z \gtrsim 20$ Å. These differences correlate with the data given in Table I for the average number of particles in layers $\langle n_l \rangle$ and layer densities $\rho_l \equiv \langle n_l \rangle / \langle \Delta z_l \rangle A$, where $\langle \Delta z_l \rangle$ is the average lth layer thickness [i.e., distance between adjacent minima in the density profile, see Figs. 1(a) and 2(a)], and A is the area of the computational cell ($A_{(001)}=321.29$ Å^2 and $A_{(111)}=310.78$ Å^2). In the liquid region Δz_l is taken, throughout the liquid, to be the thickness of the last periodic feature in the density profile $\rho(z)$. Here and elsewhere layers are numbered starting from the first dynamic layer next to the static substrate. We observe that for both systems the density is 0.086 Å^{-3} in the solid and 0.081 Å^{-3} in the liquid. However, in view of the difference between the structures of the interfacial regions, discussed above, we conclude that for the (111) system the density decrease upon transition from the crystal to the liquid is achieved by maintaining the spacing between layers along the direction normal to the interface, while the number of particles in layers decreases [see Table I, Ni(111) for $8 \leq l \leq 13$]. In contrast, for the (001) system the crystal-to-liquid transition is accompanied by a gradual increase in the layer spacings from the crystalline value while the number of particles per layer $\langle n_l \rangle$ remains roughly constant [see Table I, Ni(001) for $l \leq 12$].

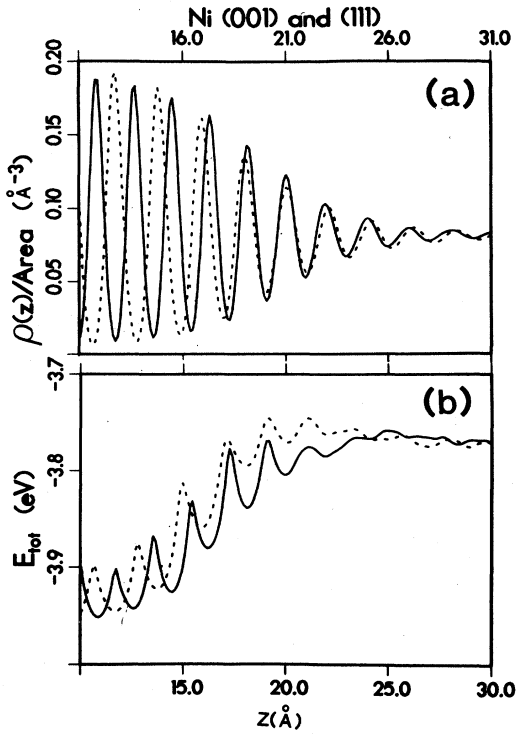

FIG. 3. Equilibrium density (a) and total energy profiles (b) vs distance z normal to the surface plane for the Ni(001), solid curve, and Ni(111), dashed, interfaces at the melting point. In drawing these figures, the profiles for the two systems were aligned such that the location of the 11th layer of the (001) system [see Fig. 1(a)], coincides with the 10th layer of the (111) system [see Fig. 2(a)]. Energies in eV and distance in Å.

These differences as well as the enhanced diffuseness of the crystal-to-melt transition region for the (001) interface reflect the larger dissimilarity between the bulk liquid structure and the local arrangement in the interfacial liquid layer at the (001) surface than at the (111) surface.[1,2,40,41]

At this juncture it is of interest to characterize in detail the degree of order in the different regions of the systems. To this end we show in Figs. 4 and 5 structure factors calculated at the equilibrium state. In these calculations

$$S_l(\mathbf{g})=\frac{1}{N_0}\sum_{i\in l} e^{i\mathbf{g}\cdot\mathbf{R}_i(t)}, \tag{2}$$

where the sum extends over particles within the spatial region assigned to the lth layer, N_0 is the number of particles per layer in the crystal [i.e., 50 and 56 for the (001) and (111), respectively], $\mathbf{g}$ is a reciprocal lattice vector, and the angular brackets in the figures denote average over time of the equilibrium trajectories. $\mathbf{g}_1$ and $\mathbf{g}_3$ are the reciprocal lattice vectors constructed from the unit cell basis vectors.[42] $\mathbf{g}_1$ lies in the plane parallel to the crystallographic orientation of the interface and $\mathbf{g}_3$ is in

the direction normal to the surface. Thus structure factors for $\mathbf{g}_1$ provide information about the degree of order parallel to the interface and those for $\mathbf{g}_3$ about order in the normal direction.

From Figs. 4(a) and 5(a) we conclude that intralayer order in both the surface parallel and normal directions decreases almost simultaneously across the transition region [compare results for $\mathbf{g}_1$ (solid circles) with those for $\mathbf{g}_3$ (empty circles)]. Note the slightly lower values for the structure factors for $\mathbf{g}_3$ indicating larger amplitudes of thermal vibrations in the normal direction and may be in part related to the existence of a static substrate and free surface in the simulations. We also observe that the transition from crystalline-to-liquid order is more gradual for the (001) system, resulting in a more diffuse interfacial region. Furthermore from the results in Figs. 4(b) and 5(b), which provide a measure of *interlayer* order between adjacent layers, in conjunction with the results for the *intralayer* order parameters [Figs. 4(a) and 5(a)], we conclude that both vary together, indicating that the degree of order in a given layer is influenced by (and is correlated to) the degree of order in the adjacent regions of the material.

Further evidence for the gradual structural transition from crystalline to liquid behavior can be obtained from the layer pair-distribution functions $G_l(r)$ shown in Figs. 6 and 7 for the Ni(001) and Ni(111) systems, respectively. The equilibrium $G_l(r)$ functions are calculated as

$$G_l(r)=\left\langle \frac{1}{n_l}\sum_{i\in l}\left[\frac{1}{(\pi r\Delta z_l)\rho_l}\sum_{\substack{j\in l\\(j\neq i)}}\delta(r_{ij}-r)\right]\right\rangle , \qquad (3)$$

where n_l and ρ_l are the instantaneous number of particles and density of layer l, respectively, the sums extend over the particles in layer l and the angular brackets denote time averaging. As seen from these figures the order in the layers decreases in a monotonic manner from crystalline-solid to liquid structure across a diffuse interface. Particularly noticeable is the gradual disappearance of the features in $G_l(r)$ corresponding to fourth, third, and second neighbors, as the interface is traversed. In addition the height of the peaks and the area under the $G_l(r)$ curves vary, which reflects the change in density across the interface (see Table I). We remark, that although the intralayer order in the interfacial regions of the systems [starting at about layers 11 and 12 for (001) and 9 and 10 for (111)] as determined from $G_l(r)$ and the

TABLE I. Equilibrium averages of number of particles $\langle n_l \rangle$, densities $\langle \rho_l \rangle$, and diffusion coefficients parallel to the surface plane $\langle D_{\parallel,l} \rangle$ [see Eq. 5(b)], in layers l for the Ni(001) and Ni(111) interfacial systems at the melting point. Density and parallel diffusion coefficients in units of Å^{-3} and Å^2/ps, respectively. Note the decrease in density upon traversing the crystal-to-melt interface and the increase in density close to the melt-to-vapor interface. Additionally, note that in the (001) system the number of particles $\langle n_l \rangle$ in the interfacial region ($12 > l \geq 9$) remains close to that in the crystal layers ($l < 9$) while in the (111) system $\langle n_l \rangle$ decreases at the interface ($13 \geq l \geq 8$). The different manners by which the two systems transform from crystal to melt correlates with the variations in spacing between layers in the interface regions of the two systems (see Fig. 3).

Dynamic layer number	Ni(001)			Ni(111)		
l	$\langle n_l \rangle$	$\langle \rho_l \rangle$ (Å^{-3})	$D_{\parallel,l}$ (Å^2/ps)	$\langle n_l \rangle$	$\langle \rho_l \rangle$ (Å^{-3})	$D_{\parallel,l}$(Å^2/ps)
1	50.0	0.086	0.00	56.0	0.086	0.00
2	50.0	0.086	0.00	56.0	0.086	0.00
3	50.0	0.086	0.00	56.0	0.086	0.00
4	50.0	0.086	0.00	56.0	0.086	0.00
5	50.0	0.086	0.00	56.0	0.086	0.00
6	50.0	0.086	0.00	56.0	0.086	0.00
7	50.0	0.086	0.00	56.0	0.086	0.00
8	50.0	0.086	0.00	54.3	0.086	0.05
9	49.6	0.084	0.01	53.7	0.085	0.22
10	49.4	0.082	0.08	51.7	0.081	0.37
11	50.4	0.081	0.17	51.5	0.081	0.40
12	50.6	0.081	0.26	51.6	0.081	0.42
13	53.2	0.081	0.35	51.6	0.081	0.46
14	53.0	0.081	0.38	54.7	0.081	0.44
15	56.5	0.081	0.39	54.4	0.081	0.40
16	56.3	0.081	0.39	54.8	0.081	0.47
17	56.2	0.081	0.39	54.6	0.081	0.56
18	56.5	0.081	0.43	54.6	0.081	0.52
19	56.4	0.081	0.52	54.6	0.081	0.51
20	56.1	0.081	0.43	54.6	0.081	0.56
21	56.1	0.081	0.45	57.1	0.085	0.60
22	56.1	0.081	0.45	29.6	0.44	0.86
23	59.1	0.085	0.51	0.5		
24	33.3	0.048	0.63			
25	0.9	0.001				

structure factors is liquidlike in nature (with vestiges of some crystalline intralayer order for that part of the transition region which is in closer proximity to the solid), the density in these interfacial regions is stratified along the directions normal to the corresponding crystalline surfaces [see Figs. 1(a) and 2(a) for the (001) and (111) interfaces, respectively], which is the reason for describing this interfacial liquid ordering phenomena as "liquid layering."[1-4] In this context we note that similar behavior was found in theoretical studies of other systems [Lennard-Jones and other simple model potentials,[1-3,10-12,14-21] as well as in theoretical studies of a simple metal[13] (Na), silicon,[23-26] and water[43] solid-to-melt interfaces] and in several experimental studies.[7] Moreover, simulations[21,24,25,27] and experiments[7] of liquid-phase epitaxial growth from the melt have revealed that liquid-layering occurs also under nonequilibrium, growth, and conditions in the propagating crystallization front, even at very high growth velocities.

To further investigate the nature of the solid-melt interface we calculated from the particle trajectories generated in the simulation the quantity

$$R_l^2(t)=\left\langle \frac{1}{n_l}\sum_{i\in l}[\mathbf{R}_i(t+\tau)-\mathbf{R}_i(\tau)]^2 \right\rangle , \tag{4}$$

where the sum includes atoms in layer l at time τ and the angular brackets indicate averaging over time origins (τ), from which the larger diffusion coefficients can be determined according to

$$D_l=\lim_{t\to\infty}\frac{R_l^2(t)}{2n_d t} , \tag{5a}$$

$$D_{\parallel,l}=\lim_{t\to\infty}\frac{R_{\parallel,l}^2(t)}{4t} \quad (n_d=2) , \tag{5b}$$

$$D_{\perp,l}=\lim_{t\to\infty}\frac{R_{\perp,l}^2(t)}{2t} \quad (n_d=1) , \tag{5c}$$

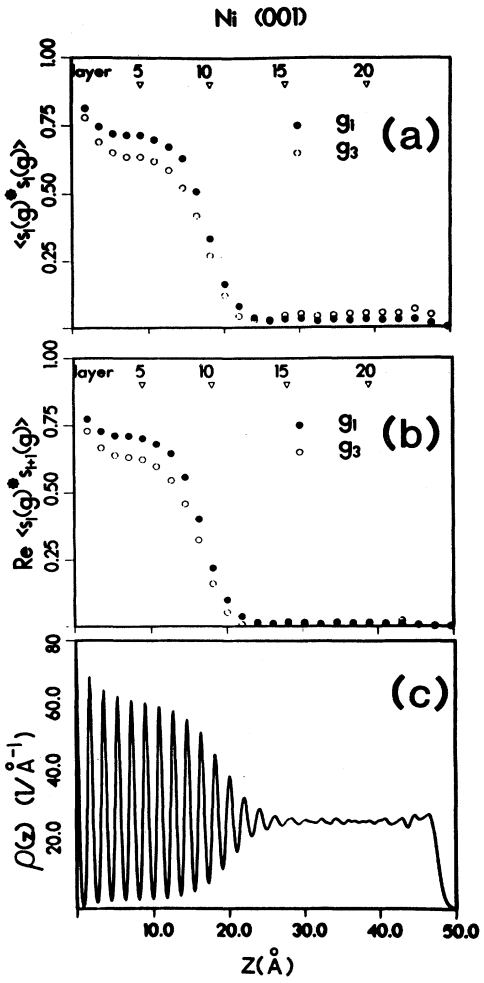

FIG. 4. Structure factors [see Eq. (2)] profiles vs distance normal to the (001) surface for the equilibrium Ni(001) system at the melting point. (a) Results for $\langle S_l^*(\mathbf{g})S_l(\mathbf{g})\rangle$; (b) results for $\mathrm{Re}\langle S_l^*(\mathbf{g})S_{l+1}(\mathbf{g})\rangle$; (c) density profile vs distance. (a) and (b) Solid and empty circles correspond to results for $\mathbf{g}_1$ (in the surface plane) and $\mathbf{g}_3$ (normal to the surface plane), respectively (Ref. 42). The location of layers is noted at the top by the triangles. The correlation between the structure factors (a) and (b) and the density profile (c) demonstrates the existence of liquid layers at the solid-melt interface.

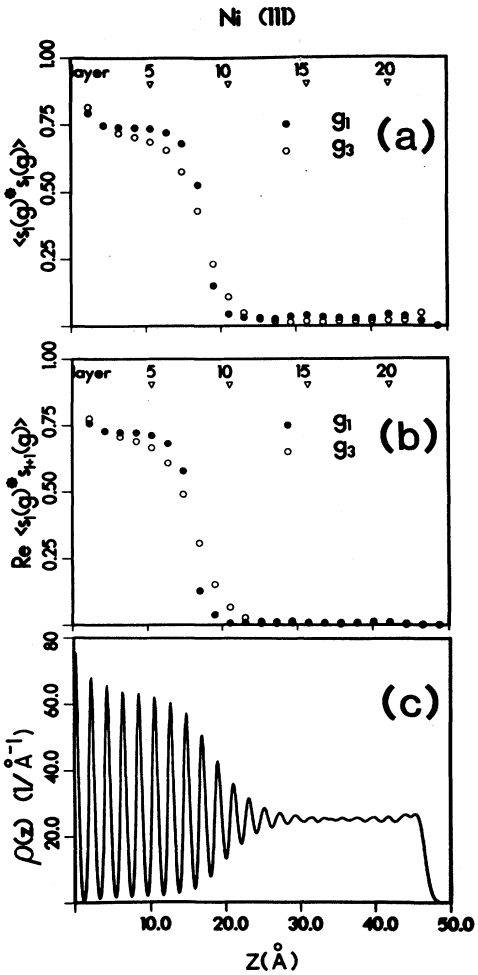

FIG. 5. Same as Fig. 4, for the Ni(111) system at the melting point. Note the sharper nature of the transition region in comparison to the Ni(001) system.

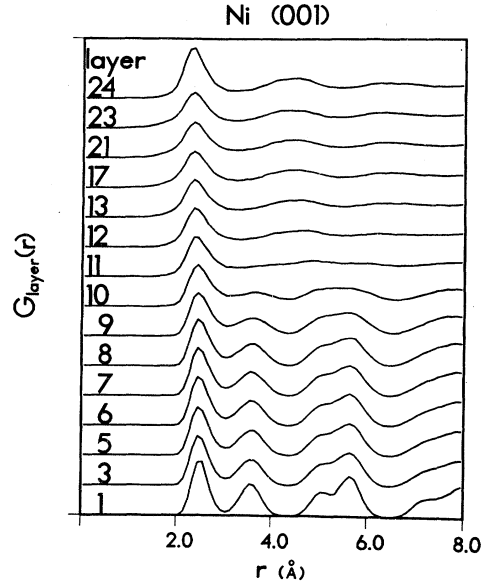

FIG. 6. Pair-distribution functions $G_{\text{layer}}(r)$ [see Eqs. (3)] in layers for the equilibrium Ni(001) system at the melting point. Layer numbers are assigned as described in the text, with layer 1 adjacent to the static substrate. Note the disappearance of crystalline features upon increasing, approaching, and traversing the crystal-to-melt interface. Note the vestiges of intralayer order, in the transition region in closer proximity to the crystalline layers.

where n_d is the dimensionality, and $R^2_{\parallel,l}(t)$, $R^2_{\perp,l}(t)$ are the components of $R^2_l(t)$ in the directions parallel and normal to the interface, respectively. Obviously the three-dimensional diffusion coefficient $D=2D_{\parallel}/3+D_{\perp}/3$.

Plots of the components of $R^2_l(t)$ for the Ni(001) and Ni(111) systems are shown in Figs. 8 and 9, respectively,

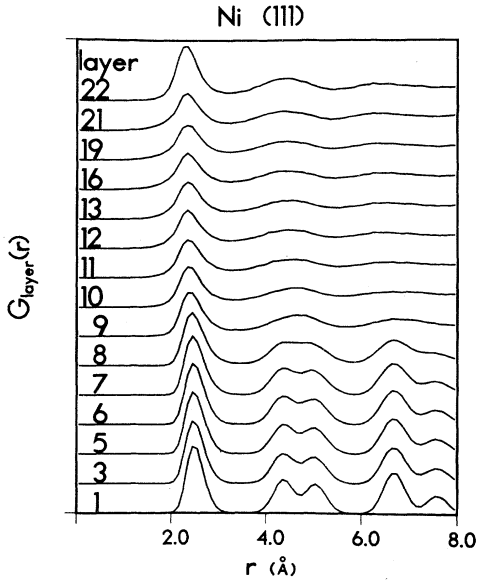

FIG. 7. Same as Fig. 6, for the Ni(111) system.

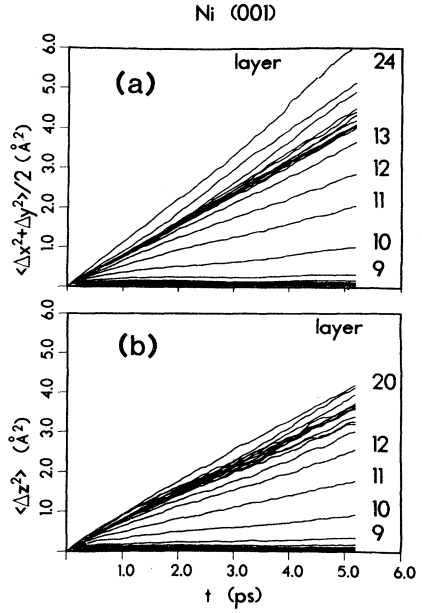

FIG. 8. The component of $R^2_l(t)$ [see Eq. (4) in a direction parallel to the surface plane $[\langle(\Delta x)^2+(\Delta y)^2\rangle/2$, (a)] and normal to it $[\langle(\Delta z)^2\rangle$, (b)] for the equilibrium Ni(001) system at the melting point. The diffusion coefficients [see Eq. (5) and Table I] are calculated from the slopes of these curves. Note the noticeably increased mobility of particles starting from layers nine to ten converging to the diffusion in the liquid region. In addition diffusion in the region close to the melt-to-vapor interface is enhanced. In addition the diffusion appears to be isotropic [note the effect of the material boundaries on the normal component (b), see text].

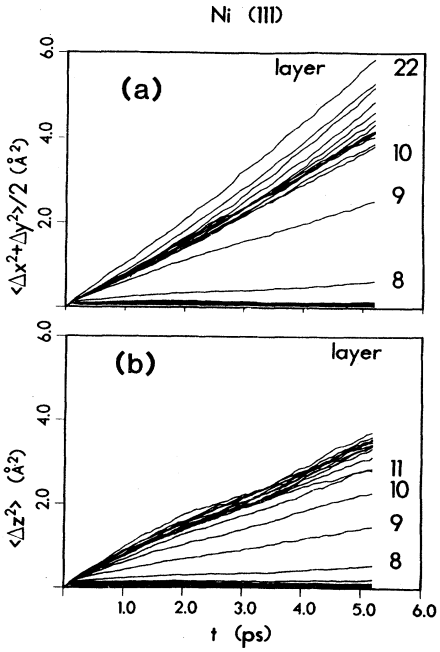

FIG. 9. Same as Fig. 8 for the Ni(111) system at equilibrium.

and values for the diffusion coefficient parallel to the interface are given in Table I. In these plots the data for the individual layers (with layer numbers assigned as above) is shown. We observe that the particle diffusion varies across the system increasing in a gradual manner from 0 in the solid to the liquid value $0.45-0.5$ Å^2 ps. Of particular interest is the correlation between the diffusion in different regions of the system and the structure in these regions. Thus for the (001) system we observe that a significant increase in diffusion occurs starting with the 10th layer, gradually increasing and converging to the bulk value at about the 14th layer (see Fig. 8 and Table I). Similarly for the (111) system significant diffusion starts at layer eight and the increase toward the bulk value is much faster, reflecting the sharper nature of the (111) solid-to-melt interface. Thus in the interface-layered region the mobility of the atoms is liquidlike in nature which together with the structural analysis given above corroborates the notion of liquid layering of that interfacial transition region. Note also that diffusion is enhanced at the liquid-vapor interfaces. We remark here that in interpreting the results for the perpendicular components of $R^2(t)$ [Figs. 8(b) and 9(b)] caution should be exercised since the particle trajectories are influenced by the presence of the solid-melt and melt-vapor interfaces. The $\langle(\Delta z)^2\rangle$ curves coincide with the $\langle[(\Delta x)^2+(\Delta y)^2]\rangle/2$ curves for short times. However, for $t \gtrsim 1.5$ ps, and particularly for liquid "layers" near either interface, the $\langle(\Delta z)^2\rangle$ curves fall below the corresponding $\langle[(\Delta x)^2+(\Delta y)^2]\rangle/2$ curves. Since the curves coincide for $t \lesssim 1.5$ ps, we believe the mobility is the same in all directions and the long-time behavior of $\langle(\Delta z)^2\rangle$ simply reflects the effects of a material interface on diffusion and of a z-dependent diffusion coefficient.

2. *Liquid-to-vapor interface*

We now turn to a discussion of the structure of the liquid-to-vapor interface. As seen from the density profiles shown in Figs. 1(a) and 2(a) this interface is characterized by a slight increase in density and a certain degree of stratification. Further evidence as to the nontrivial structure at the liquid-metal–vapor interface is provided by the energy profiles [see in particular the embedding energy and pair-potential contributions shown in Figs. 1(d), 1(e), 2(d), and 2(e)]. Accompanying (and driving) the atomic density increase at the interface are larger magnitudes of the embedding and pair-interaction energies resulting in a *net lowering* of the *total energy* at this region [see Figs. 1(c) and 2(c)]. This structural characteristic at the liquid-to-vapor interface is unique to metallic systems and is a consequence of the energetics of metallic cohesion. In the context of the parametrization of the EAM potentials[35] used in our studies we observed that due to the dominant contributions of the density-dependent embedding energy [see Eq. (1)] to the total energy of the metal $E_{\rm coh}$ the material density at the interface increases such as to increase the electron density which results in an increase in the magnitude of the embedding-energy contribution. While the repulsive energy due to the core-core interactions also increases due to the increase of density, its relative magnitude is smaller resulting in net lowering of the energy. This behavior which is in contrast to that found at the liquid-vapor interfaces of nonmetallic liquids where the density of the liquid decreases monotonically towards the vapor has been discussed previously in the context of theoretical studies of simple-metal liquid-to-vapor interfaces[31] using Monte Carlo simulations and a density-dependent effective Hamiltonian and was used by these authors to elucidate experimental results for the liquid-Hg surface.[31]

IV. SUMMARY

In this paper we have investigated the interphase interfaces of Ni using molecular-dynamics simulations and employing the embedded-atom method. Our results may be summarized as follows.

(1) Using a parametrization of the EAM potentials which was used previously in studies of liquid metals,[35] we determined the melting temperature T_m of Ni, obtaining $T_m = 1733$ K$\pm$22 K in good agreement with the experimental value[37] (1725 K). The latent heat of melting which we determined (0.19 eV/atom) is also in agreement with the experimental value[37] (0.182 eV/atom).

(2) The equilibrium crystal-to-melt interface (at the melting point) for both Ni(001) and Ni(111) is found to exhibit liquid layering, with the transition region extending over a few layers. The transition region from crystalline to liquid behavior is sharper at the Ni(111) system than in the Ni(001) system, reflecting the greater dissimilarity between the bulk liquid structure and the local arrangement in the interfacial liquid region, at the (001) surface, than at the (111) interface.[1,2,40,41]

The characteristics of the interface, coupled with the nature of cohesion in metals which is dominated by density-dependent contributions to the total energy, pose problems in extending certain density-functional approaches, such as the nonlocal weighted-density-functional approximation[44] (WDA) and that developed by Ramakrishnan and Youssouff[45] and reformulated by Haymett and Oxtoby[13] to metallic systems [in the latter method the problem of density-dependent potentials is implicit[14] by assuming that the liquid direct correlation function $C^{(2)}$ corresponding to the liquid-density potential, $\phi(\rho_l)$, is an adequate approximation to the crystal with its *different,* potential $\phi(\rho_s)$].

(3) The loss of crystalline order in traversing the crystal-to-melt interface appears to occur simultaneously for both interlayer and intralayer order.

(4) The atomic transport (diffusion) coefficient varies in a monotonic manner across the crystalline-to-melt interface, and does not seem to exhibit a marked degree of anisotropy.

(5) At the melt-to-vapor interface an increase in the liquid density and a certain amount of stratification of the liquid is observed. Underlying this behavior, in the context of the EAM potentials used in this study, is an increase in the magnitude of the embedding energy which results in a net lowering of the total energy at this region. This behavior which is in contrast to the monotonic decrease of the density at melt-vapor interfaces of non-

metallic liquid is similar to that found in theoretical studies of simple-metal liquid-to-vapor interfaces[31] and in analysis of experimental results for the liquid Hg surface.[31]

ACKNOWLEDGMENTS

This research is supported by the U.S. Department of Energy (DOE) under Grant No. DE-FG05-86ER45234.

[1]R. Mutaftschiev, in *Interfacial Aspects of Phase Transformations,* edited by B. Mutaftshiev (Reidel, Boston, 1982), p. 63.

[2]U. Landman, R. N. Barnett, C. L. Cleveland, and R. H. Rast, J. Vac. Sci. Technol. **3**, 1574 (1985).

[3]G. Rickayzen and P. Richmond, in *Thin Liquid Films,* edited by I. B. Ivanov (Dekker, New York, 1988), p. 131, and other articles in that book.

[4]See articles, in *Fluid Interfacial Phenomena,* edited by C. A. Croxton (Wiley, New York, 1986).

[5]C. A. Croxton, *Statistical Mechanics of the Liquid Surface* (Wiley, Chichester, 1980).

[6]D. P. Woodruff, *The Solid-Liquid Interface* (Cambridge University Press, London, 1973).

[7]J. H. Bilgram, Phys. Rep. **153**, 1 (1987).

[8]J. N. Israelachvili, *Intermolecular and Surface Forces* (Academic, London, 1985).

[9]J. W. Gibbs, *Collected Works* (Longmans Green, New York, 1928).

[10]Y. Singh and F. F. Abraham, J. Chem. Phys. **67**, 384 (1977).

[11]D. Hendersen, F. F. Abraham, and J. A. Barker, Mol. Phys. **31**, 291 (1976).

[12]F. F. Abraham, J. Chem. Phys. **68**, 713 (1978).

[13]A. D. J. Haymet and D. W. Oxtoby, J. Chem. Phys. **74**, 2559 (1981); **76**, 6262 (1982).

[14]W. A. Curtin, Phys. Rev. B **39**, 6775 (1989).

[15]J. Q. Broughton and G. H. Gilmer, J. Chem. Phys. **84**, 5759 (1986); **84**, 5749 (1986).

[16]J. N. Cape and L. Woodcock, J. Chem. Phys. **73**, 2420 (1980).

[17]J. Tallon, Phys. Rev. Lett. **57**, 1328 (1986).

[18]A. J. C. Ladd and L. V. Woodcock, J. Phys. C **11**, 565 (1978).

[19]J. A. Broughton, A. Bonissent, and F. F. Abraham, J. Chem. Phys. **74**, 29 (1981).

[20]F. F. Abraham, Adv. Phys. **35**, 1 (1986); J. Vac. Sci. Technol. B **2**, 534 (1984).

[21]U. Landman, C. S. Brown, and C. L. Cleveland, Phys. Rev. Lett. **45**, 2032 (1980); in *Nonlinear Phenomena at Phase Transitions and Instabilities,* edited by T. Riste (Plenum, New York, 1981).

[22]U. Landman, C. L. Cleveland, and R. N. Barnett, Phys. Rev. Lett. **49**, 790 (1982).

[23]U. Landman, W. D. Luedtke, R. N. Barnett, C. L. Cleveland, M. W. Ribarsky, E. Arnold, H. Baumgart, A. Martinez, and B. Khan, Phys. Rev. Lett. **56**, 155 (1986).

[24]U. Landman, W. D. Luedtke, M. W. Ribarsky, C. L. Cleveland, and R. N. Barnett, Phys. Rev. B **37**, 4637 (1988).

[25]W. D. Luedtke, U. Landman, M. W. Ribarsky, C. L. Cleveland, and R. N. Barnett, Phys. Rev. B **37**, 4647 (1988).

[26]F. F. Abraham, Phys. Rev. Lett. **56**, 734 (1986).

[27]See review by U. Landman, in *Computer Simulations Studies in Condensed Matter Physics,* edited by D. P. Landau, K. K. Mon, and H.-B. Schüttler (Springer, Berlin, 1988), p. 108.

[28]See, e.g., W. A. Harrison, *Pseudopotentials in the Theory of Metals* (Benjamin, Reading, Mass., 1966).

[29]R. N. Barnett, C. L. Cleveland, and U. Landman, Phys. Rev. Lett. **54**, 1679 (1985); **55**, 2035 (1985).

[30]R. N. Barnett, R. G. Barrera, C. L. Cleveland, and U. Landman, Phys. Rev. B **28**, 1667 (1983); R. N. Barnett, C. L. Cleveland, and U. Landman, *ibid.* **28**, 1685 (1983).

[31]See S. A. Rice, J. Gryko, and U. Mohanty, in Ref. 4, p. 255.

[32]For a recent review, see M. Baskas, M. Daw, B. Dodson, and S. Foiles, Mater. Res. Soc. Bull. **XIII**, 28 (1988); M. S. Daw and M. I. Baskes, Phys. Rev. B **29**, 6443 (1984); S. M. Foiles, M. I. Baskes, and M. S. Daw, *ibid.* **33**, 7983 (1986).

[33]K. W. Jacobson, J. K. Nørskov, and M. J. Puska, Phys. Rev. B **35**, 7423 (1987); J. K. Nørskov, *ibid.* **26**, 2875 (1982).

[34]P. Hohenberg and W. Kohn, Phys. Rev. B **136**, 864 (1964).

[35]S. M. Foiles, Phys. Rev. B **32**, 3409 (1985).

[36]M. Parrinello and A. Rahman, J. Appl. Phys. **52**, 7182 (1981).

[37]*Handbook of Chemistry and Physics,* edited by R. C. Weast (CRC, Cleveland, 1974).

[38]J. R. Fox and H. C. Anderson, J. Phys. Chem. **88**, 4019 (1984).

[39]E. T. Chen, R. N. Barnett and U. Landman (unpublished).

[40]J. D. Bernal and S. King, *Physics of Simple Liquids* (North-Holland, Amsterdam, 1968), p. 231; J. D. Bernal, Proc. R. Soc. London Ser. A **280**, 299 (1964).

[41]A. Bonissent and F. F. Abraham, J. Chem. Phys. **74**, 1306 (1981).

[42]The unit cell for the (001) system is defined by the primitive translation vectors: $\mathbf{a}_1=\frac{1}{2}a(1,1,0)$, $\mathbf{a}_2=\frac{1}{2}a(-1,1,0)$, and $\mathbf{a}_3=\frac{1}{2}a(1,0,1)$ and for the (111) system $\mathbf{a}_1=\frac{1}{2}a(1/\sqrt{2},\frac{3}{2},0)$, $\mathbf{a}_2=\frac{1}{2}a(-1/\sqrt{2},\frac{3}{2},0)$, and $\mathbf{a}_3=\frac{1}{2}a(1/\sqrt{2},1/\sqrt{6},2/\sqrt{3})$, where $a=3.585$ Å is the lattice parameter (fcc cube edge length) obtained from a simulation of bulk solid Ni near the melting point. In both systems $\mathbf{a}_1$ and $\mathbf{a}_2$ are parallel to the corresponding surface plane. The reciprocal lattice vectors are derived from the above as usual, i.e., $\mathbf{g}_i=2\pi(\mathbf{a}_j\times\mathbf{a}_k)/[\mathbf{a}_1\cdot(\mathbf{a}_2\times\mathbf{a}_3)]$, where (i,j,k) is the triple ordered (1,2,3) and its cyclic permutations.

[43]O. A. Karim and A. D. J. Haymet, Chem. Phys. Lett. **138**, 531 (1987).

[44]W. A. Curtin and N. W. Ashcroft, Phys. Rev. A **32**, 2909 (1985); Phys. Rev. Lett. **56**, 2775 (1986).

[45]T. V. Ramakrishnan and M. Youssouff, Phys. Rev. B **19**, 2775 (1979).